Unambiguous measurement in an unshielded microscale magnetometer with sensitivity below 1 pT/$\sqrt{\text{Hz}}$

Hamish A.M. Taylor,[*] Christopher C. Bounds, Alex Tritt, and L.D. Turner

School of Physics & Astronomy, Monash University, Melbourne, Victoria 3800, Australia

Cold-atom magnetometers exploit a dense ensemble of quanta with long coherence times to realize leading sensitivity on the micrometer scale. Configured as a Ramsey interferometer, a cold-atom sensor can approach atom shot-noise limited precision but suffers from fringe ambiguity, producing gross errors when the field falls outside a narrow predefined range. We describe how Hilbert-demodulated optical magnetometry can be realized on cold-atom sensors to provide field measurements both precise and unambiguous. Continuous reconstruction of the Larmor phase allows us to determine the dc magnetic field unambiguously in an unshielded environment, as well as measure ac variation of the field, in a single shot. The ac measurement allows us to characterize, and then neutralize, line-synchronous magnetic interference, extending reconstruction times. Using 1.6×10^6 ^{87}Rb atoms in a volume of $(68\ \mu\text{m})^3$, we measure a test field to be 86.0121261(4) μT in a single shot, achieving dc sensitivity of 380 fT in a duration of 1000 ms. Our results demonstrate that Hilbert-demodulated optical readout yields metrologically significant sensitivity without the fringe ambiguity inherent to Ramsey interferometry.

I. INTRODUCTION

Reconstructing magnetic fields at high spatial resolution and sensitivity underpins many modern applications, including medical diagnostics and imaging [1,2], and material analysis [3]. The long coherence time and small size of ultracold atomic and Bose-Einstein condensate (BEC) magnetometers makes them strong candidates for sensitive dc magnetometry [4–6] and, increasingly, ac and rf magnetometry [7,8] on the microscale. While not setting records in terms of absolute sensitivity, the volume-normalized sensitivity of these sensors approaches the proposed $\hbar$ "limit" [9], making them highly useful in applications where sub-mm spatial resolution with sufficient sensitivity is key to making precise and accurate measurements of physical and biological systems on the microscale. It is in this domain that we find high-value applications, such as semiconductor fault analysis [10], and the detection of currents during the transition of high-T_c superconductors [11]. Conventionally, these magnetometers conclude with a projective measurement of the spin populations after the sensing period, from which the spin dynamics during the sensing period can be inferred. By contrast, thermal atomic vapor magnetometers [12–17] employ continuous [18] or pulsed [19] optical readout

of the Larmor frequency of the atomic cloud in order to impute a magnetic field magnitude.

In the case of Ramsey measurement, arguably the simplest sensing protocol, the atomic spin begins in a spin-down eigenstate before being tipped transverse to the field by a resonant rf pulse produced by a local oscillator, beginning Larmor precession. After some sensing time, a second rf pulse converts the accumulated Ramsey phase—the difference between the Larmor phase and the local oscillator phase—to a population difference of the spin states. Measuring these populations allows one to infer the Larmor phase and thus an average Larmor frequency over the sensing time [7]. Smaller sensors are of course beneficial for improving spatial resolution, but absent increases in density and deleterious effects thereof, such sensors consequently have fewer spins and the precision of phase measurement is reduced. For large atom count BECs, the uncertainty of this Larmor phase measurement can be less than 10 mrad [4,20], sensing magnetic field amplitude with several orders greater precision than classical sensors of comparable volume [9]. For a given uncertainty in this phase, the uncertainty in the measured field δB scales with the reciprocal of sensing time T [18]. This favorable time scaling makes long sensing times key to improving the sensitivity δB.

The phase imputed from a single projective measurement of the final hyperfine populations is necessarily ambiguous due to the nonunique value of the Larmor

---

[*]Contact author: hamish.taylor31@gmail.com

024047-1

phase corresponding to a final population difference. A given population difference is only unique within a domain $\theta \in [-\pi/2, \pi/2]$, which is termed the principal Ramsey fringe [21,22], and thus inferring a measured field B from the measured populations requires that B lies within $\pm\pi/(2\gamma T)$ of a known value, where γ is the gyromagnetic ratio. Any violation of this assumption, referred to here as "fringe hopping," will lead to erroneous phase extraction from the spin projection, and resultant gross errors in the calculated field several orders of magnitude above that imposed by the phase uncertainty. A miscalibration of the field, or unintended drift, can lead to systematic misattribution of the fringe. More insidiously, we explain below that in the case of an unshielded magnetometer, prevalent levels of broadband magnetic field noise induce fringe-hopping errors in Ramsey measurements with long interrogation time.

Here we report unambiguous and precise magnetometry from a single, second-long interrogation of an ultracold atomic cloud. This cloud is produced in high vacuum by truncating the evaporation process in our BEC apparatus, based on a hybrid magnetic and optical-trapping configuration [23] and built across a 3×1 m optical table, the design of which is provided in detail in the previous work of our group [24]. From a continuous measurement of spin projection, we retrieve a conclusive measurement of dc magnetic field strength to nine significant figures, as well as a band-limited ac measurement of the field, from a sensing volume of 310×10^{-15} m^3. A Faraday light-matter interface continuously detects atomic spin projection, enabling a Hilbert-transform process to reconstruct the Larmor phase evolution. Hilbert-based instantaneous phase extraction has been applied to magnetometers based on NMR [25] and optical magnetometers based on shielded warm atomic vapors [26], but has thus far been applied only to large sensors, read out with correspondingly high SNR. By contrast, our microscale sensor has a factor 10^5 fewer spin quanta, and thus operates in a regime approaching the atom standard quantum limit (SQL).

II. MEASUREMENT IN NOISY ENVIRONMENTS

To consider the effect of magnetic noise on our measurement, we will begin from first principles by defining the relevant Hamiltonian. A full outline of our three-level spin-one Hamiltonian including relevant couplings is given in Appendix A, but we will lay out an illustrative two-level system here. Choosing the quantization axis to be along the magnetic field $B(t)\hat{z}$, the Zeeman Hamiltonian is $\hat{H}(t) = \gamma B(t)(\hbar/2)\hat{\sigma}_z$, where $\hat{\sigma}_z$ is the Pauli-Z operator. Considering the time-dependent Schrödinger equation, $-i\hbar\partial_t\psi = \hat{H}(t)\psi$, we may in general find the solution $\psi(t)$ through the Magnus expansion [27], $\psi(t) = \exp(\hat{\Omega}(t))\psi(0)$, where

$\hat{\Omega}(t)$ is given by

$$\hat{\Omega}(t) = \frac{1}{i\hbar}\int_0^t \hat{H}(t_1)dt_1$$
$$+ \frac{1}{2(i\hbar)^2}\int_0^t\int_0^{t_1}\left[\hat{H}(t_1), \hat{H}(t_2)\right]dt_1 dt_2 + \dots \quad (1)$$

Of note is the fact that all terms but the first are zero for any Hamiltonian, which commutes with itself at all t. For a spin-half system subject to the previously established Hamiltonian, the spin thus evolves as

$$\psi(t) = \begin{bmatrix} \exp\left(\frac{-i}{2}\int_0^t \omega(\tau)d\tau\right) & 0 \\ 0 & \exp\left(\frac{i}{2}\int_0^t \omega(\tau)d\tau\right) \end{bmatrix}\psi(0),$$
$$(2)$$

where we define the Larmor frequency $\omega(t) = \gamma B(t)$. This simplification applies for magnetic fields, which change in magnitude, but not those that change direction, which can instead generate nonadiabatic Landau-Zener transitions [28]. The result of this evolution is the creation of a phase difference between the spin states, the Larmor phase, given by

$$\phi(t) = \int_0^t \omega(\tau)d\tau = \int_0^t \gamma B(\tau)d\tau. \quad (3)$$

In a Ramsey measurement, after some duration T of free evolution, the final phase is inferred by a rotation and projection of the spin onto the quantization axis, yielding $\phi(T) = \arcsin(\langle\hat{\sigma}_z(T)\rangle)$. In the case of a linearly sensitive Ramsey measurement, in which the readout rotation is in quadrature with the initial rotation to maximize sensitivity to small field changes [29], the Ramsey phase exhibits wrapping for $|\phi| > (\pi/2)$, and as such the measured $\langle\hat{\sigma}_z\rangle$ no longer specifies the correct ϕ. Any such measurement where this phase cannot be constrained necessarily produces an ambiguous estimate [30].

In this work, we consider a stationary field $B(t) = B_0 + \epsilon_B(t)$, where $\epsilon_B(t)$ is an additive white Gaussian noise process with variance σ_B^2 and power spectral density S_{BB}, and B_0 is the static field magnitude we seek to measure. For any finite measurement time, the average $\bar{B}$ of the noise is almost never zero. Considering a measurement over an interrogation time τ as a finite sample from this distribution, this average $\bar{B}$ will itself take on a Gaussian distribution centred on zero, with standard deviation

$$\sigma_{\bar{B}} = \sqrt{\frac{S_{BB}}{2\tau}}. \quad (4)$$

Thus for a Ramsey measurement of duration τ, the phase shift as a result of the magnetic noise $\epsilon_B(t)$ will take on

a Gaussian distribution centered on zero with standard deviation

$$\sigma_\phi = \gamma \sqrt{\frac{S_{BB}\tau}{2}}. \qquad (5)$$

Consequently, the noise spectral density of the field imposes a fundamental limit on the Ramsey interrogation time for unambiguous magnetometry, when measuring with an unshielded magnetometer.

From Eq. (5), we establish a critical time for n-σ confidence of not exceeding $\phi = \pi/2$,

$$\tau_c(n) = \frac{\pi^2}{2n^2\gamma^2 S_{BB}}. \qquad (6)$$

In a typical laboratory noise environment, the noise amplitude spectral density $s_B = \sqrt{S_{BB}}$ is approximately 100 pT/$\sqrt{Hz}$ [31], and higher in close proximity to high-current power supplies. A ^{87}Rb magnetometer in such an environment has two-σ critical time $\tau_c(2) = 64$ ms, after which more than 5% of Ramsey measurements will fringe hop, leading to gross error of order $1/\gamma\tau$ in inferring the static field B_0. This error rate quickly invalidates central value estimation even from an arbitrarily large number of measurements. Considering that the coherence time of ultracold atomic magnetometers can exceed several seconds [32], this makes Ramsey measurement fundamentally unsuited to unambiguous long-period measurements on such mangetometers in the absence of shielding from external noise. Shielding ultracold atomic magnetometers has proven formidably challenging given optical access requirements and is incompatible with applications of these magnetometers to mapping fields on macroscopic samples with inherent magnetic noise sources. It is this objective of unshielded magnetometry that motivates the development of our continuous phase reconstruction protocol.

III. APPARATUS

To realize the protocol outlined in this work, we cool ^{87}Rb atoms to 1 µK, selectively catching atoms in the $|F, m_F\rangle = |1, -1\rangle$ state to produce an optically trapped cloud with a radius of 68 µm containing 1.6×10^6 atoms. Three orthogonal pairs of coils provide control over the local magnetic field. The m_F states are energetically split by an approximately 10^{-4} µT axial bias field in an arbitrarily chosen axis, with transitions between these states controlled by resonant rf radiation. Stern-Gerlach measurement of the atomic spin is achieved by releasing the trap, applying a strong magnetic field gradient, and performing time-of-flight absorption imaging of the constituent m_F populations.

The atomic spin may alternatively be continuously measured by means of an off-resonant Faraday probe beam
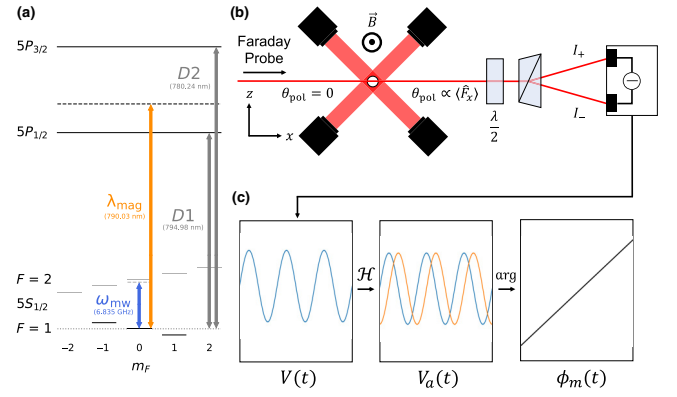

FIG. 1. Level structure, precession measurement, and Larmor phase reconstruction: the spin dynamics of the ultracold atomic cloud in the $F = 1$ hyperfine ground state are continuously probed by a far off-resonant probe at the magic wavelength λ_{mag}, with the quadratic shift nulled by off-resonant microwave dressing at frequency ω_{mw} (a). The Faraday spin-light interface couples Larmor precession in a field $B_0\hat{y}$ to the polarization rotation angle of a far-detuned probe beam focused onto the atoms (b). A balanced polarimeter (half-wave plate, Wollaston prism, and differential photodetector) transduces the Larmor signal to a voltage $V(t)$ digitized at 5 MSa/s and 16 bits. The analytic signal representation $V_a(t)$ is formed using the Hilbert transform $\mathcal{H}$, the unwrapped argument of which is the phase $\phi_m(t)$, our estimate of the Larmor phase $\phi(t)$ (c).

at the "magic wavelength" of $\lambda_{mag} = 790.03$ nm [33], between the $D1$ and $D2$ lines of ^{87}Rb, focused to a 150-µm waist to provide approximately constant illumination intensity across the atomic cloud. Due to the optical Faraday effect, this probe beam undergoes a polarization rotation proportional to the total spin projection onto the propagation direction of the probe, and this rotation is then measured by a balanced polarimeter as shown in Fig. 1. The amplitude of this polarimeter signal depends on probe power, atom count, and beam alignment, and is typically normalized by the maximum recorded value. Typically, we use a bias field of order 100 µT perpendicular to the probe-beam wave vector, maximizing the measurement of the transverse spin projection along the beam axis, which oscillates at the Larmor frequency. The quadratic Zeeman shift is suppressed by the ac Zeeman shift of an off-resonant microwave field at ω_{mw}, detuned to the red of the $|1, 0\rangle \leftrightarrow |2, 0\rangle$ clock transition, similar to the use of applied tensor light shifts to suppress the quadratic Zeeman shift in thermal atomic magnetometers [34,35]. This reduces the quadratic shift to a residual value of approximately 0.1 Hz, preventing the periodic decay and revival of the Larmor signal over our measurement lifetime [33]. The resultant polarimeter signal decays exponentially with lifetime 530 ms and remains detectable well past one second.

In order to perform dc and ac measurement of the local magnetic field, we produce a long-duration Faraday polarimeter recording of the free induction decay (FID) of Larmor precession. The initial spin eigenstate does not evolve, and no polarimeter signal is recorded. The photodetector and probe beam are switched on sequentially to characterize the electronic and optical noise spectra. The spin is then tipped into the transverse plane by a 13-μs duration resonant $\pi/2$ pulse, initiating precession at Larmor frequency $\omega(t) \approx 2\pi \times 604$ kHz. Any variation of the magnitude of the bias field appears as modulation of the Larmor frequency, making the system linearly sensitive to small changes in field in the axis of our applied bias field. While it is possible to estimate the instantaneous Larmor frequency as the numerical derivative of the instantaneous phase of the polarimeter signal, such a time-varying frequency estimate can only be averaged incoherently. In this work, we show that by reconstructing and working with the phase directly, we preserve the coherence of our measurement and exploit the favorable time scaling to achieve superior sensitivity using the long coherence time of our quantum sensor.

IV. LARMOR PHASE RECONSTRUCTION

We now consider the specific problem of estimating a stationary frequency ω in the presence of noise by linear regression to $\phi(t) = \omega t$ [36]. The reconstruction process begins with the polarimeter voltage signal

$$V(t) = A(t) \sin\left(\phi(t) + \phi_0\right) + \epsilon(t), \qquad (7)$$

where $A(t)$ is the instantaneous amplitude, $\phi(t)$ is the instantaneous Larmor phase, $\epsilon(t)$ is an additive white Gaussian noise process with variance σ^2 band limited at the Nyquist frequency corresponding to a sampling rate $f_s = 5$MSa/s. The reference phase ϕ_0 accounts for rf, atomic, and electro-optical delays between the local oscillator and digitization of the polarimeter signal. The SNR at any given time is defined as the full-bandwidth SNR, given by $\mathrm{SNR} = A_{\mathrm{rms}}^2/\sigma^2 = A^2/2\sigma^2$, as is standard in relevant signal-processing literature [36], not to be confused with the postfilter SNR defined in certain other literature on Faraday polarimetry [33,37]. The polarimeter signal is then filtered with a zero-phase sixth-order Butterworth band-pass filter around the Larmor frequency, giving

$$V_{\mathrm{pb}}(t) = A(t) \sin\left(\phi(t) + \phi_0\right) + \epsilon_{\mathrm{pb}}(t), \qquad (8)$$

where $A(t)$ and $\phi(t)$ are unchanged under the assumption that the signal power is entirely contained within the passband, which will be verified in experiment in Sec. VI. As this filtering is applied postexperiment, we can make use of a noncausal zero-phase filter, which does not significantly alter the signal phase near the center of the band.

The purpose of this prefiltering is to reduce the threshold SNR required for achieving the Cramer-Rao lower bound (CRLB) for phase-based frequency estimation by least-squares regression [36,38], as will be described in Sec. VII. This has a typical threshold $\mathrm{SNR_{thr}}$ of 6 dB. Other estimators have been considered [39–41], but their computational complexity makes them ill suited for applications with high sample counts.

Considering a passband with equivalent noise bandwidth Δf_{pb}, the threshold SNR is reduced by $\Delta \mathrm{SNR_{thr}} = 10 \log_{10}(2\Delta f_{\mathrm{pb}}/f_s)$ dB, and the maximum allowable equivalent noise bandwidth to maintain the CRLB is given by

$$\Delta f_{\mathrm{pb}} = \frac{f_s}{2} \times \frac{\mathrm{SNR}}{10^{3/5}}. \qquad (9)$$

The passband of the filter transmits only a small fraction of the input power, which is overwhelmingly dominated by photon shot noise. The frequency of the Larmor precession can be easily identified in the polarimeter power spectrum by comparison to the pretip spectrum outlined in Sec. II, allowing us to correctly center the passband. The band-filtered signal V_{pb} is then used to produce an analytic signal representation of the polarimeter measurement,

$$V_a(t) = V_{\mathrm{pb}}(t) + i\mathcal{H}\left[V_{\mathrm{pb}}\right](t), \qquad (10)$$

where $\mathcal{H}[\cdot]$ represents the Hilbert transform. Details of the Hilbert transform and analytic signal representation are well presented elsewhere [42]; its utility in this application is the conversion of a real signal with conjugate positive and negative frequency components to a complex-valued signal with only positive frequency components and a well-defined phase. Of note, so long as the Larmor signal power is entirely captured within the passband, no signal information is lost or distorted in the conversion to the filtered analytic signal representation $V_a(t)$.

The analytic representation is then recast in polar form as $V_a(t) = V_m(t) e^{i\phi_m(t)}$, where $V_m(t) = |V_a(t)|$ is the instantaneous amplitude envelope and $\phi_m(t) = \arg(V_a(t))$ is the (wrapped) instantaneous phase of the signal. As our Nyquist frequency well exceeds our Larmor frequency, this phase may be trivially unwrapped using NumPy's unwrap routine [43]. This unwrapped instantaneous phase is a measurement of the relative Larmor phase, and it is the evolution of this phase as governed by Eq. (3) that allows us to perform dc and ac magnetometry with the system. The measurement and reconstruction workflow of our magnetometer is shown in Fig. 1.

V. AC MAGNETOMETRY

While our field model thus far has considered only a constant magnetic field with additive white Gaussian noise, there are additional field contributions that must be considered in real environments. As an unshielded sensor,

our apparatus is sensitive to magnetic fields from adjacent electronics. In our laboratory, low-frequency magnetic interference is dominated by line-synchronous oscillations at the power line fundamental of 50 Hz, and its odd harmonics. In a typical environment, the fundamental component has amplitude of order 100 nT [31], with the 150-Hz harmonic of order 30 nT, and higher harmonics correspondingly weaker. A common technique to mitigate this interference is to synchronize the measurement to the line cycle and limit interrogation times to be much shorter than the line period $\tau \ll 20$ ms. This greatly limits the sensitivity of the magnetometer in cases such as ours where the coherence time exceeds one second. When interrogating for $\tau \gg 20$ ms, we resolve this interference as frequency modulation of the Larmor carrier frequency, allowing us to extract interference amplitudes from the phase modulation. The reconstruction of the Larmor phase over a duration of 320 ms, or 16 line cycles, in the unshielded laboratory environment is shown in Fig. 2.

From our 320-ms reconstruction, we extract the RMS amplitudes of the 50-, 150-, and 250-Hz field harmonic components of 41.92(3), 10.88(9), and 2.0(1) nT, respectively, by least-squares regression of a harmonic interference model to the phase function. The ac sensitivity is quantified and discussed in Sec. VII. The phase-reconstruction duration is limited by the declining polarimeter SNR as scattering of probe light removes atoms from the cloud. In theory, the reconstruction SNR can be improved by a reduction in sensor bandwidth through tightening the passband, initially chosen to be

5 kHz; however, there exists a minimum bandwidth below which we impinge on the signal band. The amplitude of the harmonic components determines the frequency deviation of the Larmor signal, and sets this minimum bandwidth, estimated at 2.5 kHz peak-to-peak on previous work with this apparatus [44] using Carson's rule, which provides a good approximation of the spectral support of wide-band frequency-modulated signals [45]. Strong field fluctuations lead to large variations in Larmor frequency, requiring a wider pass bandwidth, which admits more photon shot noise, and thus bringing forward the time by which the polarimeter SNR is insufficient for accurate phase reconstruction.

The corresponding minimum SNR for least-squares phase estimation considering our initially chosen pass bandwidth of 5 kHz is −21 dB as provided by (9). This limits the reconstruction duration in the case of the measurement shown in Fig. 2 to approximately 500 ms before we can no longer achieve the CRLB through least-squares estimation. Additionally, once the SNR has fallen significantly below this threshold, phase reconstruction may fail entirely due to phase-unwrapping errors, leading to discontinuities in the reconstruction. For this reason, it is imperative to reduce frequency modulation from magnetic interference to allow for the narrowest possible passband, and hence the longest possible measurement time.

VI. FEED-FORWARD NOISE CANCELLATION

As magnetic interference from electrical equipment is a common problem in metrology experiments, there already exists a body of literature discussing methods of suppressing it. These range from simple feed-forward control cancelling periodic noise using prior field recordings [7,46] to complex feedback mechanisms combining measurements from several secondary sensors in the vicinity of the primary sensor [47,48]. While feedback control is effective against periodic *and* nonperiodic noise, the aforementioned secondary sensor methods necessarily measure the field at some distance from the atoms, and struggle to neutralize the spatially varying interference arising from multiple sources. On the other hand, using the atomic sensor as the input for feedback control [49] necessarily sacrifices limited quantum resources. While capable of providing strong suppression of ac magnetic interference in stable environments, feed-forward noise cancellation in ultracold atoms to date has relied on performing a long series of calibration measurements [7,50], making the system vulnerable to short-term drifts in interference amplitude and phase.

Acknowledging that the dominant contribution to the modulation is the quasistationary line-synchronous interference, we may use our measurement of the local magnetic environment to perform feed-forward noise cancellation by producing a complementary ac field. This
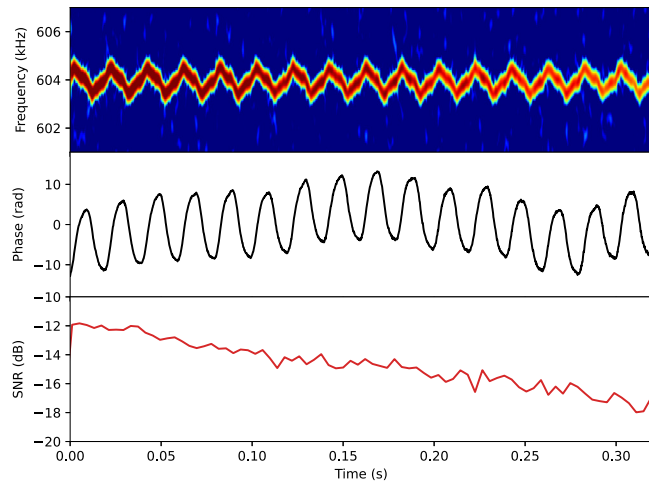
FIG. 2. Continuous spin measurement: the polarimeter signal, a frequency-modulated sinusoid as seen in its spectrogram (top) is transformed into an analytic signal representation via the Hilbert transform. The phase function (middle) extracted from this is shown with the linear term removed to make plain the frequency modulation. The full-bandwidth SNR of the polarimeter signal (bottom) decays exponentially over the reconstruction time of 320 ms, due to off-resonant scattering and spin dephasing.

complementary field is synchronized to the electrical line phase at the beginning of each measurement by an external trigger, and is produced by small, single-turn shim coils with a diameter of 6 cm, fastened to the interior surface of a cylindrical polyvinyl chloride mount and placed coaxially with the bias coils. The coil currents are controlled by an analog output card, which feeds a voltage-controlled current supply, with an overall system time constant of 40 μs, allowing arbitrary ac magnetic fields to be produced with a maximum amplitude of 6.61(3) μT and bandwidth of 10 kHz. The amplitudes and phases of the modulation terms extracted from the reconstructed phase evolution in our unshielded atomic cloud [Fig. 2 (middle)] calibrate the noise cancellation. The effects of this noise suppression are readily apparent in the power spectrum of the polarimeter signal: where the Larmor resonance is initially spread over a wide range of frequencies, suppression of the line-synchronous interference results in a narrow resonance with no defined sidebands. This allows us to tighten the bandpass filter from 5 kHz to 500 Hz while keeping all of the resonance within the flat range of the passband. The polarimeter signal power spectra and the relevant bandpass filter gains are shown in Fig. 3.

Figure 4 shows the polarimeter signal, reconstructed phase, and SNR, now with feed-forward noise cancellation enabled, over almost one second of interrogation time. In comparison with Fig. 2, the line harmonics are now imperceptible in the spectrogram, and indeed there is no

FIG. 4. Continuous spin measurement with feed-forward noise cancellation: the spectrogram (top) now exhibits a stable carrier frequency without visible frequency modulation. The phase function residuals (middle) demonstrate random walk behavior with discontinuities appearing at later times in the reconstruction due to phase-wrapping errors when using the wider bandwidth of 5 kHz (gray), but successful reconstruction at the tighter 500-Hz bandwidth (black). Frequency measurement by phase estimation achieves the Cramer-Rao bound so long as the SNR remains above the threshold for the respective bandwidths (bottom).
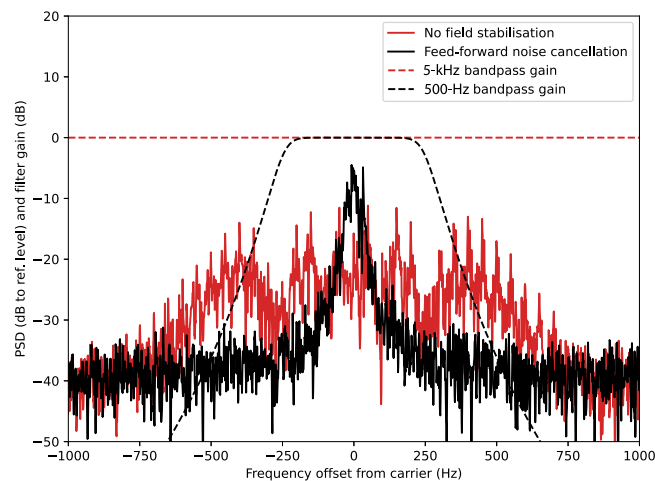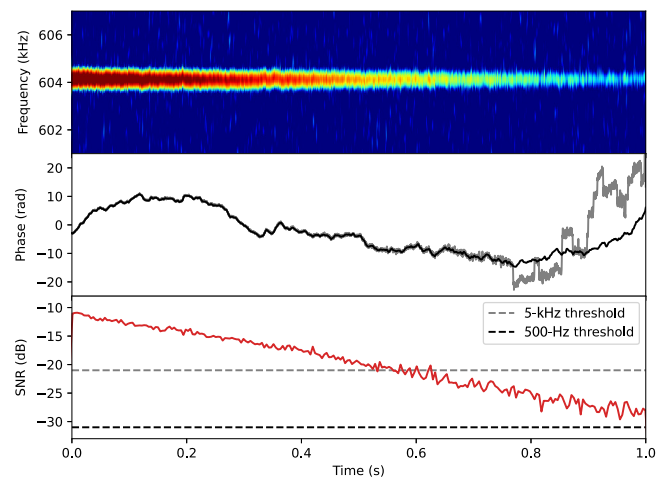

FIG. 3. Feed-forward noise cancellation reduces the bandwidth occupied by the Larmor signal: due to harmonic interference, the power spectral density (PSD) of the Larmor signal in a nonstabilized environment (red) has significant signal power at deviations up to 750 Hz from the carrier frequency. With feed-forward noise cancellation (black) this deviation is reduced by almost an order of magnitude, permitting reduction of the filter bandwidth from 5 kHz (dashed red) to 500 Hz (dashed black). The PSDs share the same reference level. Note that the 5-kHz bandpass filter gain rolls off by only 0.3 dB across the displayed range.

visible harmonic fluctuation in the residual phase. This reduction of the pass bandwidth from 5 kHz to 500 Hz permits the reconstruction time to be extended out to the full 1000 ms while maintaining sufficient SNR to achieve the CRLB. As a result, the phase retrieved from the narrower filter [black trace in Fig. 4 (middle)] shows no sign of phase unwrapping errors across the full reconstruction time, whereas the phase retrieved from the original filter (gray trace) manifests a series of such errors once the SNR falls significantly below threshold beyond approximately 750 ms.

The efficacy of feed-forward noise cancellation depends almost entirely on the stability of the local magnetic environment. Changes in the power draw of high-current devices (such as motors, amplifiers, and air conditioning equipment) cause shifts in the phase and amplitude of the line harmonics, leading to reduced noise cancellation until another ac magnetometry calibration measurement is performed. The measurement and reconstruction process, from the beginning of trap loading to completion of postprocessing, takes less than one minute, allowing rapid recalibration of noise cancellation in the event of a change in the magnetic environment. In practice, a calibration measurement is performed daily to account for changes in the position or current draw of local equipment.

We quantify the field stability by analyzing the magnetic power spectral density $S_{BB}(f)$ in the sub-300-Hz band, estimated by a periodogram of the derivative of the Larmor
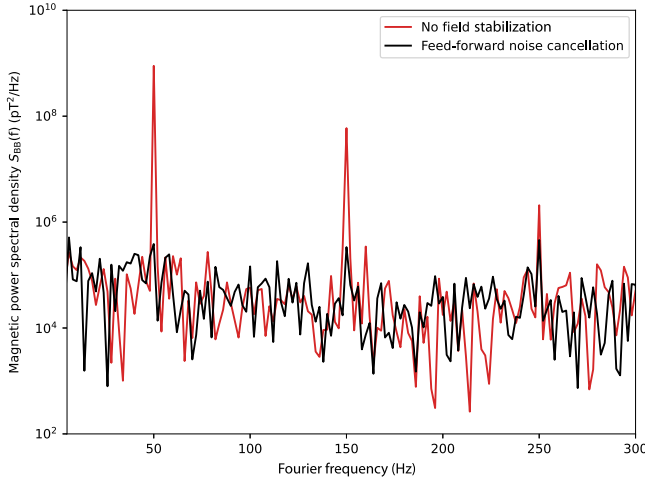
FIG. 5. Feed-forward noise cancellation eliminates line harmonics from the magnetic noise spectrum: the magnetic power spectral density is reconstructed from single-shot Faraday polarimeter signals with (black) and without (red) feed-forward noise cancellation. The Fourier-limited frequency resolution of this spectrum is 2 Hz.

phase as per Eq. (3). Additionally, we define the equivalent RMS magnetic noise amplitude

$$\delta B_{\text{noise}} = \sqrt{\int_0^{f_{\text{max}}} S_{\text{BB}} \, df} \,, \tag{11}$$

which for the laboratory field is measured to be 44.4 nT for a f_{max} of 300 Hz. Feed-forward noise cancellation reduces this by a full order of magnitude to $\delta B_{\text{noise}} = 4.4$ nT representing a 20.1-dB reduction in interference in the sub-300-Hz band; this accounts for the significant reduction in the bandwidth occupied by the Larmor signal shown in Fig. 3. Figure 5 shows the measured magnetic noise power spectral density S_{BB}, confirming that the laboratory environment is dominated by the 50-, 150-, and 250-Hz line interference harmonics.

Making use of feed-forward noise cancellation, the line-synchronous interference is suppressed to become only marginally resolvable against the white-noise background of $250 \, \text{pT}/\sqrt{\text{Hz}}$. Owing to drifts in the grid frequency of up to 100 mHz [51], feed-forward noise cancellation is most effective for the fundamental frequency of 50 Hz, and less effective for higher harmonics, for which this frequency error is multiplied. It is useful to clarify that this figure of $s_{\text{B}} = 250 \, \text{pT}/\sqrt{\text{Hz}}$ is not a sensitivity, and merely characterizes the stability of the background field. This magnetic noise spectral density is marginally higher than typical values reported in a laboratory environment [31], and is likely a result of our use of high-current equipment in relatively close proximity to the apparatus. The 2σ critical time predicted by Eq. (6) for this magnetic noise spectral

density is only 10 ms, limiting Ramsey measurement duration to a small fraction of the Zeeman coherence time of our ultracold atomic sensing platform.

VII. PHASE-RETRIEVAL DC MAGNETOMETRY

We realize dc magnetometry by performing a Faraday polarimetry measurement of the FID under feed-forward noise cancellation. The Larmor phase is then reconstructed using the same method as described in Sec. III. With the nearly complete removal of the line-synchronous modulation, it is expected that the Larmor phase will increase linearly, and as such we now perform a least-squares regression of the reconstructed phase function $\phi_m(t)$ to the linear model $\phi_m(t) = \gamma B_{\text{est}} t + \phi_{\text{est}}$. In the case of a truly static magnetic field, the phase residual is simply the white Gaussian photon and atom shot noise $\epsilon_{pb}(t)$ of the polarimeter voltage signal $V_{pb}(t)$ imputed as phase noise. However, in the case of an unshielded apparatus with appreciable fluctuations in the magnetic field, the phase noise has a colored spectrum, as shown in Fig. 6. This phase power spectral density can be decomposed into two terms, a colored noise term reflecting underlying noise in the measured magnetic field, and a white-noise term as a result of imputing photon and atom shot noise as phase fluctuations, with the crossover frequency found at 800 Hz. The measured photon shot noise background across the 5 MSa of a single recording was found to be indistinguishable from additive white Gaussian noise by the Kolmogorov-Smirnov test ($D = 4.3 \times 10^{-4}$, $p = 0.35$).
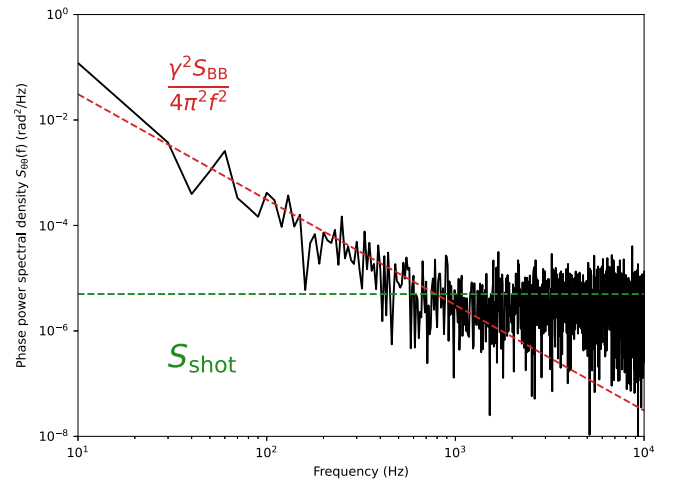

FIG. 6. Phase power spectral density: the power spectrum of the Larmor phase residuals under feed-forward noise cancellation. Above the corner frequency of 800 Hz, the noise spectrum is white as a result of photon shot noise. Below this frequency, the noise floor is dominated by red phase noise due to approximately white environmental magnetic field noise. The Fourier-limited frequency resolution of this spectrum is 10 Hz.

As shown in Fig. 5, the magnetic power spectral density is approximately white under feed-forward noise cancellation, corresponding to the red noise in the phase power spectral density. Considering this, we define the model

$$S_{\phi\phi}(f) = \frac{\gamma^2 S_{\mathrm{BB}}}{4\pi^2 f^2} + S_{\mathrm{shot}}, \tag{12}$$

where S_{BB} is the magnetic power spectral density as defined previously, and $S_{\mathrm{shot}} = 2/(f_s \mathrm{SNR})$ for $f < \omega/(2\pi)$ [25]. Thus, the phase noise power asymptotically increases as the Fourier limit frequency tends to zero, and would be unbounded in the limit $\tau \to \infty$. As interrogation time increases, commensurately more low-frequency noise contributes to the phase noise, becoming the dominant contribution for $\tau \gg 1$ s. The sensitivity of the field estimate produced by this reconstruction is fundamentally limited by the regression error, resulting in a sensitivity

$$\delta B_{\mathrm{dc}} = \frac{2\,\delta\phi}{\gamma\tau^{\frac{3}{2}}} \sqrt{\frac{3}{f_s}}, \tag{13}$$

where $\delta\phi$ is the RMS amplitude of the phase residuals; the derivation of this expression is shown in Appendix B. Considering the noise spectra shown in Fig. 6 with a measurement duration of 1 s and associated Fourier limit frequency of 1 Hz, the majority of the total phase noise power is a result of detector noise, and as such we consider the detector noise-limited regime identified in Appendix B. In this limit, in terms of SNR, the dc sensitivity is given by

$$\delta B_{\mathrm{dc}} = \frac{1}{\gamma\tau^{\frac{3}{2}}} \sqrt{\frac{12}{f_s \mathrm{SNR}}}. \tag{14}$$

This metric illuminates the superior time scaling achieved by a continuous phase-coherent measurement, motivating longer phase reconstruction duration. With the performance of our magnetometer characterised, we now perform precise dc magnetometry by continuous phase-reconstruction under feed-forward noise cancellation. In an experimental run, a series of shots were performed measuring the 86.03(4) μT static field of the laboratory environment. The high variability of this measured field is due to quasi-dc changes as a result of a rail line in proximity to our laboratory, as has been independently verified by a commercial flux-gate magnetometer. Taking a single shot in this series, we obtain Figs. 3–5, with a phase reconstruction spanning a sensing duration of $\tau_s = 1000$ ms, in a sensing volume of $310 \times 10^{-15}\,\mathrm{m}^3$. From this reconstruction, we measure an average field of 86.0121261(4) μT, with an estimation-limited sensitivity of $\delta B_{\mathrm{dc}} = 380$ fT, and an inferred detector-limited sensitivity of $\delta B_{\mathrm{dc}} = 359(7)$ fT calculated from Eq. (14) using the weighted average SNR of $-20.2(1)$ dB, as

described in Appendix B. This achieves superior sensitivity in such a volume when compared to other quantum platforms such as bulk nitrogen-vacancy centers in diamond, and approaches the sensitivity per unit volume reported in work on other (ambiguous) measurement protocols in ultracold atoms and BEC [9]. This also marks a significant improvement over comparable frequency-based measurements using a Faraday measurement of ultracold atoms, which achieved a sensitivity of 141 pT in a sensing duration of 5 ms on a condensate of 3×10^5 atoms, for which the measurement duration was limited by ac modulation of the measured field rather than coherence lifetime [33]. With regards to ac sensing, the ac sensitivity can also be characterised by imputing an equivalent magnetic noise for a given amplitude of phase noise [26]. Considering this, we find the expression

$$\delta B_{\mathrm{ac}} = \frac{2\pi f}{\gamma \sqrt{f_s\,\tau\,\mathrm{SNR}}}. \tag{15}$$

Using the initial SNR of -11.1 dB achieved for measurement time $\tau < 10$ ms this corresponds to an initial bandwidth-normalized ac sensitivity of $\delta B_{\mathrm{ac}}\sqrt{T} = 230 \times f\,\mathrm{fT}/\sqrt{\mathrm{Hz}}$. Unlike dc sensitivity, the bandwidth-normalized ac sensitivity of this sensor does not scale with increased measurement time. Naturally, to successfully measure an ac signal at frequency f, the pass bandwidth must exceed $2f$: as the probability of phase-reconstruction errors increases with pass bandwidth, this establishes a maximum sensing bandwidth. Taking the maximum allowable passband width to be the same as that defined in Eq. (10), we find a maximum passband of 48.8 kHz, and consequently a baseband ac sensing range of up to 24.4 kHz. The ac bandwidth of the sensor can be improved by increasing the SNR of the Faraday signal, however this would require a brighter probe beam, reducing the scattering lifetime of the atoms and negatively impacting the dc sensitivity.

The competitive dc and ac sensitivity of this sensor up to frequencies of several kHz, combined with its small active sensing volume, suggests that it will be able to meet the demands of microscale sensing applications in both biological and materials sciences, particularly if used as a scanning probe of magnetic structure [6]. The high-vacuum environment in which the ultracold atomic vapor is held does present a barrier to measurement of vacuum-incompatible samples, such as live cells, and as such the utility of our sensor is at present limited to measuring magnetically active samples, which can tolerate at least a low-vacuum environment. The minimally destructive nature of the Faraday measurement also gives rise to the prospect of using it to supplement other measurements, such as a projective interferometry measurement, to provide a more complete picture of the spin dynamics over the sensing duration.

VIII. CONCLUSION

We have developed a continuous phase-reconstruction protocol on a microscale ultracold atomic sensor allowing precise, unambiguous dc measurement and ac measurement of magnetic field in a noisy environment. Measuring unshielded in Earth's field, the magnetometer resolves nine significant figures of the dc field magnitude in a single shot, undeterred by field drifts of up to several microtesla between shots. Additionally, we have demonstrated suppression of local magnetic interference by over 20 dB by feed-forward control. This sensor fulfills the requirements of rapid, calibration-free, unambiguous, and unshielded magnetometry needed to realize magnetic microimaging of electrophysiological function, surface condensed-matter physics, and chemical structure on the cellular scale.

APPENDIX A: SPIN-1 DYNAMICS WITH MICROWAVE COUPLING

As outlined in Sec. II, our alkali spinor is a three-level spin-1 system with free evolution governed by the diagonal Hamiltonian $\hat{H}(t)$. Owing to the precision of the measurement performed here, we consider this system in full generality using the Breit-Rabi equation for Zeeman energy eigenvalues in $J = 1/2$ states [52], given by

$$E_{F,m}(B) = \frac{-E_{\text{HFS}}}{2(2I+1)} + g_I \mu_B m B$$
$$\pm \frac{E_{\text{HFS}}}{2}\sqrt{1 + \frac{4mx}{2I+1} + x^2}, \quad (A1)$$

where $x = ((g_J - g_I)\mu_B B)/E_{\text{HFS}}$ is the dimensionless magnetic field magnitude, and $F = I \pm J$ defines the signs, so that the minus is adopted for our $F = 1$ manifold, for $I = 3/2$ in ^{87}Rb. In the above equations, μ_B is the Bohr magneton, E_{HFS} is the ground-state hyperfine splitting, g_J and g_I are the fine structure, and nuclear Landé factors, respectively, and m is the magnetic quantum number. In the absence of any other couplings, this results in an $F = 1$ manifold Hamiltonian given by

$$\hat{H} = \begin{bmatrix} E_{1,+1}(B) & 0 & 0 \\ 0 & E_{1,0}(B) & 0 \\ 0 & 0 & E_{1,-1}(B) \end{bmatrix}, \quad (A2)$$

where henceforth we suppress explicit time dependence. As the Hamiltonian is diagonal and thus commutes with

itself at all times, we may define a Larmor frequency from the Magnus expansion as done in Sec. II, giving

$$\omega(t) = \frac{E_{1,+1}(B) - E_{1,-1}(B)}{2\hbar}, \quad (A3)$$

and additionally define a quadratic Zeeman shift

$$q(t) = \frac{E_{1,+1}(B) + E_{1,-1}(B) - 2E_{1,0}(B)}{2\hbar}. \quad (A4)$$

Typically, the Breit-Rabi equation is only expanded to second order when considering weak-field dynamics, leading to

$$\omega = \frac{(5g_i - g_j)\mu_B}{4\hbar}B + \mathcal{O}(B^3) \approx \gamma_0 B, \quad (A5)$$

and

$$q = \frac{(g_i - g_j)^2 \pi \mu_B^2}{8E_{\text{HFS}}\hbar^2}B^2 + \mathcal{O}(B^4) \approx q_0 B^2, \quad (A6)$$

where $\gamma = 2\pi \times -7.02369\,\text{GHz/T}$ and $q_0 = 2\pi \times 7.189\,\text{GHz/T}^2$ are the zero-field gyromagnetic ratio and quadratic Zeeman shift, respectively, using known values [53]. Outside the low-field limit, or where high precision is required, the cubic term in Eq. (A5) can also be included, resulting in a $c_0 = 44.24\,\text{GHz/T}^3$ shift to the Larmor frequency. If this term is included, we may no longer decompose the Larmor frequency in terms of a constant gyromagnetic ratio γ_0. However, as the Larmor frequency remains a monotonic function of field, we may instead define a "running" gyromagnetic ratio $\gamma(B)$, defined such that

$$\omega(t) = \gamma(B) \times B. \quad (A7)$$

During "free" evolution of the spin, it interacts with two off-resonant radiation fields: the Faraday probe and the microwave driving. The scalar, vector, and tensor light shifts as a result of the Faraday probe can be made arbitrarily small through use of a "magic-zero wavelength" and precise control of polarisation [33], leaving the off-resonant microwave coupling as the only additional term to consider in the Hamiltonian. A microwave source detuned from the $|1, 0\rangle$ and $|2, 0\rangle$ states cancels the quadratic Zeeman shift by inducing an ac Zeeman shift given by

$$q_{\text{mw},0} = -\frac{\Omega_{\text{mw}}^2}{4\Delta_{\text{mw}}}, \quad (A8)$$

where $\Omega_{\text{mw}} \approx 2\pi \times 6\,\text{kHz}$ and $\Delta_{\text{mw}} \approx 2\pi \times 150\,\text{kHz}$ are the microwave Rabi frequency, and detuning from the clock transition, respectively. In the limit $\omega \gg \Delta_{mw}$, this shift is only substantial for the $|1, 0\rangle \leftrightarrow |2, 0\rangle$ transition,

however when we consider fields of order $100\ \mu\text{T}$, the Zeeman shift is of the same order as the detuning, resulting in appreciable ac Zeeman shifts for the $m = \pm 1$ states. These shifts are given by

$$q_{\text{mw},\pm 1} = -\frac{\hbar\Omega_{\text{mw}}^2}{4\hbar(\Delta_{\text{mw}} - (E_{2,\pm 1} - E_{2,0}) + (E_{1,\pm 1} - E_{1,0}))}, \tag{A9}$$

with shifts on the ± 1 states differing in both magnitude and direction. This leads to additional nonlinear terms in $E_{F,m}(B)$, which must be included at the field magnitude and desired measurement precision in this work. As such, we define modified eigenenergies including the microwave shifts, by

$$E'_{F,m}(B) = E_{F,m}(B) + q_{\text{mw},m}, \tag{A10}$$

and recompute the Larmor frequency

$$\omega(t) = \frac{E'_{1,+1}(B) - E'_{1,-1}(B)}{2\hbar}, \tag{A11}$$

and similarly the quadratic Zeeman shift

$$q(t) = \frac{E'_{1,+1}(B) + E'_{1,-1}(B) - 2E'_{1,0}(B)}{2\hbar}. \tag{A12}$$

Away from the resonance $\Delta_{\text{mw}} = \omega$, the Larmor frequency is a monotonic function of B, allowing us to take the decomposition

$$\omega(t) = \gamma_{\Omega,\Delta}(B) \times B, \tag{A13}$$

where $\gamma_{\Omega,\Delta}(B)$ is the modified running gyromagnetic ratio, which explicitly depends on the parameters of the microwave coupling as well as the field. The microwave frequency is locked to a precision reference, and contributes negligible error, and the Rabi frequency at the atoms is determined experimentally by nulling the total quadratic shift at a given B through a process of iterative optimization.

Thus, with known Ω_{mw}, Δ_{mw}, and relevant atomic parameters, frequency estimation can provide accurate field estimation at precisions which require inclusion of the nonlinear elements of the Zeeman splitting. The running gyromagnetic ratio depends only weakly on B, and thus the decomposition used in Eq. (A13) illustrates the near-linear relation between field and Larmor frequency.

APPENDIX B: SENSITIVITY

In order to quantify the dc sensitivity of a regression error-limited field estimate from phase reconstruction, we define the sensitivity as

$$\delta B_{\text{dc}} = \frac{\sigma_\omega}{\gamma}, \tag{B1}$$

where σ_ω is the standard error in the angular frequency estimate retrieved from least-squares regression of a time series $[t_i, \phi_i]$ to a linear model over a sensing time τ. The standard error in such an estimate is a well-established result in regression theory, given by

$$\sigma_\omega = \sqrt{\frac{\sigma_r^2}{\sum_{i=0}^N (t_i - \bar{t})^2}}, \tag{B2}$$

with the standard deviation about the regression σ_r equal to

$$\sigma_r = \sqrt{\frac{\sum_{i=0}^N (\phi_i - \hat{\phi}_i)^2}{N - 2}}, \tag{B3}$$

where $\hat{\phi}_i$ is the regression estimate for ϕ_i. The factor $N - 2$ is present due to the loss of two statistical degrees of freedom. In the limit of large samples,

$$\lim_{N\to\infty} \sigma_r = \delta\phi. \tag{B4}$$

Additionally in this limit, we may take the continuum limit of the sum over t_i, giving

$$\sum_{i=0}^N (t_i - \bar{t})^2 = f_s \int_0^\tau \left(t - \frac{\tau}{2}\right)^2 dt = f_s \frac{\tau^3}{12}. \tag{B5}$$

We may now rewrite Eq. (B2) as

$$\sigma_\omega = \frac{2\,\delta\phi}{\tau^{\frac{3}{2}}} \sqrt{\frac{3}{f_s}}, \tag{B6}$$

and equivalently rewrite Eq. (B1) as

$$\delta B_{\text{dc}} = \frac{2\,\delta\phi}{\gamma\tau^{\frac{3}{2}}} \sqrt{\frac{3}{f_s}}. \tag{B7}$$

The residual phase variance $\delta\phi^2$ is the sum of variance arising from shot noise in the detector and variance as a result of noise in the actual field,

$$\delta\phi^2 = \delta\phi_{\text{shot}}^2 + \delta\phi_{\text{field}}^2. \tag{B8}$$

As previously discussed, shot noise is imputed as additive white Gaussian noise in our phase reconstruction, giving rise to an equivalent full-bandwidth phase variance of $\delta\phi^2_{\text{shot}} = 1/\text{SNR}$ [25], while the field phase variance is given by

$$\delta\phi^2_{\text{field}} = \int_{\frac{1}{\tau}}^{\infty} \frac{\gamma^2 S_{\text{BB}}}{4\pi^2 f^2} df = \frac{\gamma^2 S_{\text{BB}}\tau}{4\pi^2}. \tag{B9}$$

Thus,

$$\delta\phi = \sqrt{\frac{1}{\text{SNR}} + \frac{\gamma^2 S_{\text{BB}}\tau}{4\pi^2}}. \tag{B10}$$

In the detector noise-limited regime, where $\delta\phi^2_{\text{shot}} \gg \delta\phi^2_{\text{field}}$, this reduces to

$$\delta\phi = \sqrt{\frac{1}{\text{SNR}}}. \tag{B11}$$

Combining this with Eq. (B7), we find our governing intrinsic sensitivity equation

$$\delta B_{\text{dc}} = \frac{1}{\gamma\tau^{\frac{3}{2}}} \sqrt{\frac{12}{f_s\,\text{SNR}}}. \tag{B12}$$

It can additionally be shown that this achieves the Cramer-Rao bound for phase-based frequency estimation. The Cramer-Rao bound on the variance of the unbiased estimator of angular frequency is given [54] by

$$\sigma^2_{\hat{\omega}} = \frac{12}{\text{SNR}\,N(N^2-1)} \left(\frac{\text{rad}}{\text{sample}}\right)^2, \tag{B13}$$

which in the large sample limit is

$$\sigma^2_{\hat{\omega}} = \frac{12 f_s^2}{\text{SNR}\,N^3}. \tag{B14}$$

Putting this in terms of previously defined quantities using $N = f_s\tau$ and $\omega = \gamma B$, this becomes

$$\sigma^2_{\hat{B}} = \frac{12}{\gamma^2 f_s\,\text{SNR}\,\tau^3}, \tag{B15}$$

or as a sensitivity,

$$\sigma_{\hat{B}} = \frac{1}{\gamma\tau^{\frac{3}{2}}} \sqrt{\frac{12}{f_s\text{SNR}}}, \tag{B16}$$

exactly equivalent to Eq. (B12).

That least-squares regression in the high SNR limit achieves the Cramer-Rao bound for phase-based frequency estimation is an established result in information theory [36], shown here for completeness. In the case of a decaying SNR, as is the case for our Faraday measurement, the reconstructed phase estimates are heteroskedastic, and as such we estimate the Larmor frequency via a weighted least-squares regression, which is the best linear unbiased estimator [55]. Though the statistics of this regression are more involved, a weighted average SNR, which takes into account the decay lifetime and measurement duration, can be found, from which the detector-limited sensitivity can be calculated as per Eq. (B12).

---

[1] J. Belfi, G. Bevilacqua, V. Biancalana, S. Cartaleva, Y. Dancheva, and L. Moi, Cesium coherent population trapping magnetometer for cardiosignal detection in an unshielded environment, J. Opt. Soc. Am. B **24**, 2357 (2007).

[2] S. Xu, V. V. Yashchuk, M. H. Donaldson, S. M. Rochester, D. Budker, and A. Pines, Magnetic resonance imaging with an optical atomic magnetometer, Proc. Natl. Acad. Sci. **103**, 12668 (2006).

[3] J. W. Wilson, G. Y. Tian, and S. Barrans, Residual magnetic field sensing for stress measurement, Sens. Actuators A **135**, 381 (2007).

[4] M. Vengalattore, J. M. Higbie, S. R. Leslie, J. Guzman, L. E. Sadler, and D. M. Stamper-Kurn, High-resolution magnetometry with a spinor Bose-Einstein condensate, Phys. Rev. Lett. **98**, 200801 (2007).

[5] N. Behbood, F. Martin Ciurana, G. Colangelo, M. Napolitano, M. W. Mitchell, and R. J. Sewell, Real-time vector field tracking with a cold-atom magnetometer, Appl. Phys. Lett. **102**, 173504 (2013).

[6] F. Yang, A. J. Kollár, S. F. Taylor, R. W. Turner, and B. L. Lev, Scanning quantum cryogenic atom microscope, Phys. Rev. Appl. **7**, 034026 (2017).

[7] Y. Eto, H. Ikeda, H. Suzuki, S. Hasegawa, Y. Tomiyama, S. Sekine, M. Sadgrove, and T. Hirano, Spin-echo-based magnetometry with spinor Bose-Einstein condensates, Phys. Rev. A **88**, 031602(R) (2013).

[8] Y. Cohen, K. Jadeja, S. Sula, M. Venturelli, C. Deans, L. Marmugi, and F. Renzoni, A cold atom radio-frequency magnetometer, Appl. Phys. Lett. **114**, 073505 (2019).

[9] M. W. Mitchell and S. Palacios Alvarez, Quantum limits to the energy resolution of magnetic field sensors, Rev. Mod. Phys. **92**, 021001 (2020).

[10] K. Chang, A. Eichler, J. Rhensius, L. Lorenzelli, and C. L. Degen, Nanoscale imaging of current density with a single-spin magnetometer, Nano Lett. **17**, 2367 (2017). pMID: 28329445.

[11] E. Berg, E. Fradkin, E.-A. Kim, S. A. Kivelson, V. Oganesyan, J. M. Tranquada, and S. C. Zhang, Dynamical layer decoupling in a stripe-ordered high-T_c superconductor, Phys. Rev. Lett. **99**, 127003 (2007).

[12] W. C. Griffith, S. Knappe, and J. Kitching, Femtotesla atomic magnetometry in a microfabricated vapor cell, Opt. Express **18**, 27167 (2010).

[13] I. K. Kominis, T. W. Kornack, J. C. Allred, and M. V. Romalis, A subfemtotesla multichannel atomic magnetometer, Nature **422**, 596 (2003).

[14] D. Sheng, S. Li, N. Dural, and M. V. Romalis, Subfem-totesla scalar atomic magnetometry using multipass cells, Phys. Rev. Lett. **110**, 160802 (2013).

[15] H. B. Dang, A. C. Maloof, and M. V. Romalis, Ultrahigh sensitivity magnetic field and magnetization measurements with an atomic magnetometer, Appl. Phys. Lett. **97**, 151110 (2010).

[16] A. L. Bloom, Principles of operation of the rubidium vapor magnetometer, Appl. Opt. **1**, 61 (1962).

[17] W. Chalupczak, R. M. Godun, S. Pustelny, and W. Gawlik, Room temperature femtotesla radio-frequency atomic magnetometer, Appl. Phys. Lett. **100**, 242401 (2012).

[18] D. Budker and M. V. Romalis, Optical magnetometry, Nat. Phys. **3**, 227 (2007).

[19] A. Borna, T. R. Carter, P. DeRego, C. D. James, and P. D. D. Schwindt, Magnetic source imaging using a pulsed optically pumped magnetometer array, IEEE Trans. Instrum. Meas. **68**, 493 (2019).

[20] K. S. Hardman, P. J. Everitt, G. D. McDonald, P. Manju, P. B. Wigley, M. A. Sooriyabandara, C. C. N. Kuhn, J. E. Debs, J. D. Close, and N. P. Robins, Simultaneous precision gravimetry and magnetic gradiometry with a Bose-Einstein condensate: A high precision, quantum sensor, Phys. Rev. Lett. **117**, 138501 (2016).

[21] C. L. Degen, F. Reinhard, and P. Cappellaro, Quantum sensing, Rev. Mod. Phys. **89**, 035002 (2017).

[22] N. Shiga and M. Takeuchi, Locking the local oscillator phase to the atomic phase via weak measurement, New J. Phys. **14**, 023034 (2012).

[23] Y.-J. Lin, A. R. Perry, R. L. Compton, I. B. Spielman, and J. V. Porto, Rapid production of ^{87}Rb Bose-Einstein condensates in a combined magnetic and optical potential, Phys. Rev. A **79**, 063631 (2009).

[24] A. Wood, *Spinor Bose-Einstein condensates in magnetic field gradients*, Ph.D. thesis, Monash University, 2017.

[25] R. Hong *et al.*, Systematic and statistical uncertainties of the Hilbert-transform based high-precision FID frequency extraction method, J. Magn. Reson. **329**, 107020 (2021).

[26] N. Wilson, C. Perrella, R. Anderson, A. Luiten, and P. Light, Wide-bandwidth atomic magnetometry via instantaneous-phase retrieval, Phys. Rev. Res. **2**, 013213 (2020).

[27] S. Blanes, F. Casas, J. A. Oteo, and J. Ros, The Magnus expansion and some of its applications, Phys. Rep. **470**, 151 (2009).

[28] C. C. Bounds, J. P. Duff, A. Tritt, H. A. M. Taylor, G. X. Coe, S. J. White, and L. D. Turner, Quantum spectral analysis by continuous measurement of Landau-Zener transitions, Phys. Rev. Lett. **132**, 093401 (2024).

[29] J. M. Taylor, P. Cappellaro, L. Childress, L. Jiang, D. Budker, P. R. Hemmer, A. Yacoby, R. Walsworth, and M. D. Lukin, High-sensitivity diamond magnetometer with nanoscale resolution, Nat. Phys. **4**, 810 (2008).

[30] G. Waldherr, J. Beck, P. Neumann, R. Said, M. Nitsche, M. Markham, D. Twitchen, J. Twamley, and F. Jelezko, High-dynamic-range magnetometry with a single nuclear spin in diamond, Nat. Nanotechnol. **7**, 105 (2011).

[31] P. J. M. Wöltgens and R. H. Koch, Magnetic background noise cancellation in real-world environments, Rev. Sci. Instrum. **71**, 1529 (2000).

[32] C. Deutsch, F. Ramirez-Martinez, C. Lacroûte, F. Reinhard, T. Schneider, J. N. Fuchs, F. Piéchon, F. Laloë, J. Reichel, and P. Rosenbusch, Spin self-rephasing and very long coherence times in a trapped atomic ensemble, Phys. Rev. Lett. **105**, 020401 (2010).

[33] M. Jasperse, M. J. Kewming, S. N. Fischer, P. Pakkiam, R. P. Anderson, and L. D. Turner, Continuous Faraday measurement of spin precession without light shifts, Phys. Rev. A **96**, 063402 (2017).

[34] K. Jensen, V. M. Acosta, J. M. Higbie, M. P. Ledbetter, S. M. Rochester, and D. Budker, Cancellation of nonlinear Zeeman shifts with light shifts, Phys. Rev. A **79**, 023406 (2009).

[35] W. Chalupczak, A. Wojciechowski, S. Pustelny, and W. Gawlik, Competition between the tensor light shift and nonlinear Zeeman effect, Phys. Rev. A **82**, 023417 (2010).

[36] M. L. Fowler, Phase-based frequency estimation: A review, Digit. Signal Process. **12**, 590 (2002).

[37] G. A. Smith, S. Chaudhury, and P. S. Jessen, Faraday spectroscopy in an optical lattice: A continuous probe of atom dynamics, J. Opt. Soc. Am. B **5**, 323 (2003).

[38] D. Kim, M. Narasimha, and D. Cox, An improved single frequency estimator, IEEE Signal Process. Lett. **3**, 212 (1996).

[39] M. Luise and R. Reggiannini, Carrier frequency recovery in all-digital modems for burst-mode transmissions, IEEE Trans. Commun. **43**, 1169 (1995).

[40] M. Fitz, Further results in the fast estimation of a single frequency, IEEE Trans. Commun. **42**, 862 (1994).

[41] Z. Zhao, S. Särkkä, J. Sjölund, and T. B. Schön, Probabilistic estimation of instantaneous frequencies of chirp signals, IEEE Trans. Signal Process. **71**, 461 (2023).

[42] R. N. Bracewell, *Fourier Transform and its Applications* (McGraw-Hill, New York, 1999).

[43] C. R. Harris *et al.*, Array programming with NumPy, Nature **585**, 357 (2020).

[44] R. P. Anderson, M. J. Kewming, and L. D. Turner, Continuously observing a dynamically decoupled spin-1 quantum gas, Phys. Rev. A **97**, 013408 (2018).

[45] J. Carson, Notes on the theory of modulation, Proc. IEEE **51**, 893 (1963).

[46] B. Merkel, K. Thirumalai, J. E. Tarlton, V. M. Schäfer, C. J. Ballance, T. P. Harty, and D. M. Lucas, Magnetic field stabilization system for atomic physics experiments, Rev. Sci. Instrum. **90**, 044702 (2019).

[47] D. Platzek, H. Nowak, F. Giessler, J. Röther, and M. Eiselt, Active shielding to reduce low frequency disturbances in direct current near biomagnetic measurements, Rev. Sci. Instrum. **70**, 2465 (1999).

[48] X.-T. Xu, Z.-Y. Wang, R.-H. Jiao, C.-R. Yi, W. Sun, and S. Chen, Ultra-low noise magnetic field for quantum gases, Rev. Sci. Instrum. **90**, 054708 (2019).

[49] R. Zhang, Y. Ding, Y. Yang, Z. Zheng, J. Chen, X. Peng, W. Teng, and H. Guo, Active magnetic-field stabilization with atomic magnetometer, Sensors **20**, 4241 (2020).

[50] A. Smith, B. E. Anderson, S. Chaudhury, and P. S. Jessen, Three-axis measurement and cancellation of background

magnetic fields to less than 50 µG in a cold atom experiment, J. Phys. B: At., Mol. Opt. Phys. **44,** 205002 (2011).

[51] R. Panel, *The Frequency operating standard*, Tech. Rep. (Australian Energy Market Commission, 2023).

[52] G. Breit and I. I. Rabi, Measurement of nuclear spin, Phys. Rev. **38,** 2082 (1931).

[53] D. A. Steck, Rubidium 87 D line data (2003), http://steck.us/alkalidata.

[54] S. M. Kay, in *Prentice Hall Signal Processing Series* (Prentice Hall, Englewood Cliffs, N.J, 2013).

[55] A. C. Aitken, IV.—on least squares and linear combination of observations, Proc. R. Soc. Edinb. **55,** 42 (1936).